Effect of Transition Metal and Different Rare-Earth Inhibitors-Based Sol–gel Coatings on Corrosion Protection of Mild Steel

Aarti Gautam[1,2] · K. R. C. Soma Raju[1] · K. V. Gobi[2] · R. Subasri[1]

Abstract

Autonomous healing coatings based on encapsulation of corrosion inhibitors into nanocontainers is gaining a lot of attention. In the present work, coating formulations based on hybrid organic–inorganic sol–gel coatings impregnated with chrome-free corrosion inhibitors such as Zr^{4+} (Z) and various rare-earth elements (RE: Ce^{3+}, La^{3+}, Gd^{3+}, Er^{3+}) were investigated on mild steel substrates. Effects for both the direct addition of corrosion inhibitor (Z/RE) into the matrix sol and the addition of halloysite nanoclay encapsulated corrosion inhibitor (Z/RE-H) were evaluated. To evaluate the coating performance and self-healing action of different corrosion inhibitors, various characterization techniques such as potentiodynamic polarization studies, electrochemical impedance spectroscopy, micro-Raman spectroscopy, salt spray test and scanning electron microscopy-elemental analysis were used. Electrochemical studies and salt spray tests clearly confirm that coatings derived from a direct addition of corrosion inhibitors to the matrix sol result in an excellent performance. The current densities of coatings based on direct addition of Zr^{4+} and Ce^{3+} were very low, in the order of 10^{-10} and 10^{-9} A/cm^2, respectively, when compared to other RE and all Z/RE-H coatings, which exhibited a current density of 10^{-6} A/cm^2. Micro-Raman analysis confirmed the self-healing action of zirconium and cerium-based coatings.

Keywords Cationic corrosion inhibitors · Sol–gel coatings · Corrosion protection · Mild steel · Self-healing

1 Introduction

The high mechanical strength, ductility and low cost make mild steel (MS) a valuable structural material for construction/infrastructure industry, home appliances, oil industries, and automobile industries. Although, MS is highly efficient in several aspects, its surface gets corroded very fast under aggressive environmental conditions. Though corrosion may not have an immediate effect, it can lead to a decrease in mechanical strength, deterioration in physical appearance, and premature failures which demand partial or complete replacement of frameworks, thereby increasing global gross expenditure [1]. Corrosion-related destruction has resulted in a negative impact on the industrial sector as well as the

safety of human lives [2]. To minimize this effect, paint technology was used in the initial days to shield the surface of the metal from direct contact with the harsh environment. Paints serve as a barrier against various corrosive reactants [3]. Hexavalent chrome based conversion coatings help to suppress corrosion by slowing the rate of reaction, but they are banned globally by REACH (Registration, Evaluation, Authorization and Restrictions of Chemicals) regulation due to their toxicity [4]. Hybrid sol–gel coatings are the best alternative for these chromate-based conversion coatings. Sol–gel coatings have low curing temperatures, good adhesion, durability, and flexibility, which improve the corrosion and mechanical resistance of the coatings [5]. To increase the protection efficiency of these hybrid sol–gel coatings, corrosion inhibitors are mixed into the sol and applied on mild steel substrates [6]. A variety of organic and inorganic corrosion inhibitors have been investigated for this purpose. Organic corrosion inhibitors comprising N, O, P, and S heteroatoms are most popular since they tend to form a metal–ligand bond with the mild steel surface [7, 8]. In recent years, inorganic corrosion inhibitors based on transition metals and rare-earth elements (RE) have gained

✉ R. Subasri
subasri@arci.res.in

1 Centre for Sol-Gel Coatings, International Advanced Research Centre for Powder Metallurgy and New Materials (ARCI), Balapur, Hyderabad 500005, India

2 Department of Chemistry, National Institute of Technology Warangal, Warangal 506004, India

interest. The reason behind switching from organic to inorganic corrosion inhibitors is because of their abundance and due to low loading requirement in the coating matrix. They are environmental friendly and their indigestion or inhalation by human beings does not possess any harmful effect. Furthermore, use of rare-earth corrosion inhibitors is considered as economically competitive, as some of them are relatively abundant in nature [9]. Considering all these facts, it is quite reasonable to use inorganic corrosion inhibitors for corrosion protection of Mg, Al alloys and mild steel [10]. The mechanism of action of rare-earth corrosion inhibitors is through blocking of cathodic sites by forming an insoluble layer of their oxides/hydroxides. The film thus formed acts as a barrier to corrosive media [11, 12]. The direct addition of these corrosion inhibitors is sometimes beneficial for instant corrosion protection. However, encapsulation becomes necessary to increase the coating performance for an extended period as it helps slow and controlled release of corrosion inhibitors. Various encapsulating agents such as nanotubes, nanorods, nanoclay, etc. are widely used based on their chemical structures and morphology [13, 14]. The choice of nanocontainers is purely based on their compatibility with the corrosion inhibitor and with the metal substrate. The pre-loaded nanocontainers can sense the corrosive environment and thereby releases the corrosion inhibitors due to certain triggering mechanism. These encapsulated nanocontainers minimize the leaching process by controlled release of the corrosion inhibitors [15]. Different nanocontainers such as layer-by-layer polymeric shell [16], polymer-based nanocontainers [17], ion exchange resins [18], layered double hydroxides [19], carbon nanotube, nanoclays such as montmorillonite [20] and halloysite nanotubes [21], etc. are used. Our previous work concluded that the halloysite nanoclay (HNT) works more efficiently as a nanocontainer when compared to layer-by-layer nanocontainers for mild steel [22]. Halloysite nanotubes($Al_2Si_2O_5(OH)_4 \cdot nH_2O$) have a layered aluminosilicate tubular structure with a hollow lumen inside. HNTs have an external diameter of 40–60 nm, internal diameter of 10–15 nm and length of 700–1000 nm. Presence of empty lumen makes it an effective nanocontainer for loading the corrosion inhibitor inside the lumen of the HNTs instead of intercalating in between the alumina and silicate layers [13, 23].

So far, there are no reports on the use of the wide range of RE as well as a comparison of their protection efficiency among themselves and with the transition metal-based corrosion inhibitor, Zr^{4+}. In addition, due to the emerging importance of self-healing coatings based on encapsulating inhibitors into nanocontainers, effects of the direct addition and the encapsulation into HNT followed by homogenizing in the sol–gel matrix were investigated. Hence, in the current study, we have loaded different inorganic corrosion inhibitors such as Zr^{4+}, La^{3+}, Ce^{3+}, Er^{3+} and Gd^{3+} into HNTs and

compared the corrosion protection efficiency of coatings based on direct addition and encapsulated inhibitors into the matrix sol using various electrochemical and spectroscopic techniques.

2 Experimental

2.1 Materials

The hybrid silica matrix sol was prepared using 3-(Glycidoxypropyl) trimethoxysilane (GPTMS from Alfa Aesar, USA, chemical purity—97%) and tetraethyl orthosilicate (TEOS from Sigma Aldrich, USA, chemical purity—98%) as precursors. Zirconium n-propoxide (Sigma Aldrich, USA), cerium nitrate ($Ce(NO_3)_3$, SRL, India), lanthanum nitrate ($La(NO_3)_3$), gadolinium acetate ($Gd(CH_3CO_2)_3$), and erbium nitrate ($Er(NO_3)_3$) (Alfa Aesar, USA) were used as the source for the cationic corrosion inhibitors. Methacrylic acid (MAA, ABCR GmbH & Co., Germany) Halloysite nanotubes (HNT from Sigma Aldrich, USA) were used as the nanocontainers. The elemental composition in weight% of MS coupons obtained from a local supplier was C: 0.18, Mn: 0.58, Si: 0.25, P: 0.018, S: 0.037, and Fe: ~98.9. MS coupons with the dimensions of 2.5 cm×2.5 cm×0.3 cm were used as substrates.

2.2 Synthesis of Sol and Coating Deposition

The matrix sol was synthesized by mixing 56.50 g of GPTMS with 16.12 g of TEOS (molar ratio of 3.1:1.0). Then, 1.72 ml of 0.1 M HCl was added dropwise to the mixture with continuous stirring for 2 h at room temperature to catalyze the reaction. The synthesized matrix sol was used to prepare various sols containing different corrosion inhibitors. For this, 2 wt% of each corrosion inhibitor was added into 25 g of matrix sol individually. The sols were labelled as follows: matrix sol as Mat, zirconium n-propoxide added matrix sol as ZS, lanthanum nitrate + matrix sol as LS, cerium nitrate + matrix sol as CS, gadolinium acetate + matrix sol as GS, and erbium nitrate + matrix sol as ES. For the study of encapsulation, 2.17 g of the above-mentioned corrosion inhibitors were individually loaded into HNTs and then subsequently 2 wt% loaded HNTs were mixed into matrix sol as reported earlier [24]. Coatings from these sols were labelled as ZHS, LHS, CHS, GHS and EHS, respectively. The direct addition of corrosion inhibitors into matrix sol is abbreviated as Z/RE and after encapsulation into HNT as Z/REH. Prior to coating application or deposition, the MS coupons were polished using 600, 800 and 1000 grit abrasive paper. To remove excess dirt, grease and impurities, the MS coupons were soaked in acetone and subjected to ultra-sonication for 30 min prior

to coating application. The coatings were generated using a dip-coater (EPG GmbH, Germany) at a withdrawal rate of 6 cm/min. The coated samples were kept for curing in an oven for 1 h at 130 °C.

2.3 Characterization

2.3.1 Characterization of Inhibitor-Loaded Nanocontainers

Initially, HNTs and inhibitor-loaded HNTs were studied. A ZEISS Gemini 500 Scanning electron microscope equipped with an energy-dispersive X-ray spectrophotometer (EDS) was used to examine surface morphology and elemental composition. SEM images were recorded under a vacuum condition of 7.5×10^{-5} Pa with acceleration potentials of electron gun kept in the range of 5–20 kV. FTIR spectra of as-received HNT and inhibitor-loaded HNT were obtained using the Vertex 70, Bruker Optik GmbH, Germany. An X-ray diffractometer (Bruker AXS D8 Advance, USA) was used to perform X-ray diffraction (XRD) in the 2θ range of 5°-100° with a step size of 0.1°.

2.3.2 Coating Characterization

The coating thickness of all the coated substrates was measured with a PosiTector® 6000 (De Felsko Corporation, USA). The tape-pull off test was carried out using a multi hatch gauge (BEVS 2203, China) in accordance with ISO standard 2409, and the substrates were then examined under an optical microscope (BX51M). A Kruss GmbH drop shape analyser was used to measure the water contact angle (WCA). The contact angle was calculated using the tangent method and the DSA II software.

An electrochemical system from CH instruments (Model CHI 604E, USA) was used to perform electrochemical impedance spectroscopy (EIS) and potentiodynamic polarization studies (PPS) on bare and coated MS substrates after soaking them in 0.6 M sodium chloride solution for 1 h. EIS was employed to interpret the coating properties. The quantitative data obtained using EIS is relatively fast and authentic; therefore, the impedance measurement helps in analyzing the coating properties in terms of adherence and durability. To study the effect of inhibition and self-healing action yet, an another powerful technique was used i.e., potentiodynamic polarization measurement. This technique is destructive in which the external voltage is applied to break the coating and observe the inhibition action in terms of current density and corrosion potential. Polarization method is widely explored in determining the change in current density and corrosion potentials of thin film coatings such as sol–gel coatings.

A three-electrode-set up was used with a reference saturated calomel electrode, an auxiliary Pt plate electrode, and bare/coated MS substrates employed as working electrode. An amplitude of 0.01 V AC signal was used to record electrochemical impedance data from 100 kHz to 0.01 Hz. The impedance data for bare, CS and all other coatings, whether direct addition or encapsulated inhibitor coated MS substrates, were fitted using three different equivalent electrical circuits as shown in Fig. 1. These circuits correspond to different interfacial behaviours of bare and coated MS. Figure 1a depicts the electrical circuit used for bare MS, whereas (b) and (c) corresponds to CS and other RE direct and encapsulated sol-coated MS substrates, respectively, where R_s is for solution resistance, R_{coat} is the coating resistance, R_{ct} is charge transfer resistance, R_{diff} is the diffusion

Fig. 1 Equivalent circuits for **a** bare MS; **b** all coatings except CS and **c** CS coatings
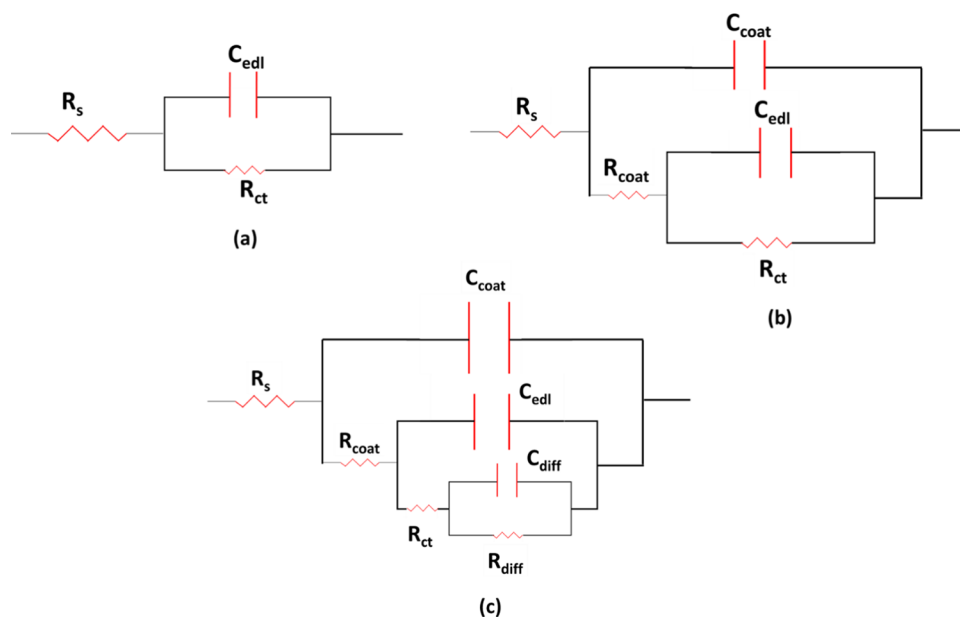
resistance, C_{coat} is coating capacitance, C_{edl} is capacitance due to electrical double layer and C_{diff} is capacitance due to diffusion.

ZSimpWin® and CH604E® software were used to extract the electrochemical fit parameters. To calculate the pseudo-capacitance or capacitance (C) values for the data fitted using constant phase elements (CPEs), the following equation was used:

$$C = (CPE, Yo * R)^{\frac{1}{n}}/R$$

where n and Y_o are surface heterogeneity factor ($0.5 < n < 1$) and admittance of the CPE, respectively. To assure the reproducibility of the results, four individual measurements ($n = 4$) were performed for each system.

Polarization range of ± 300 mV was applied around the open circuit potential (OCP) at a scanning rate of 1 mV/s. The polarization resistance values were calculated with a slight over potential of ± 30 mV with respect to OCP.

The salt spray test was carried out on the scribed coated and bare MS coupons in accordance with ASTM B117 for 5 h. The exposed samples were observed under FESEM to observe the surface morphology of the scribed area. EDS was also carried out to confirm the presence of corrosion inhibitors in the scribed area. Micro Raman Spectroscopy technique was also employed (Labram Micro Raman Spectrometer) to confirm the presence of inhibitor and

self-healing action of the corrosion inhibitor in the scribed area.

3 Results and Discussion

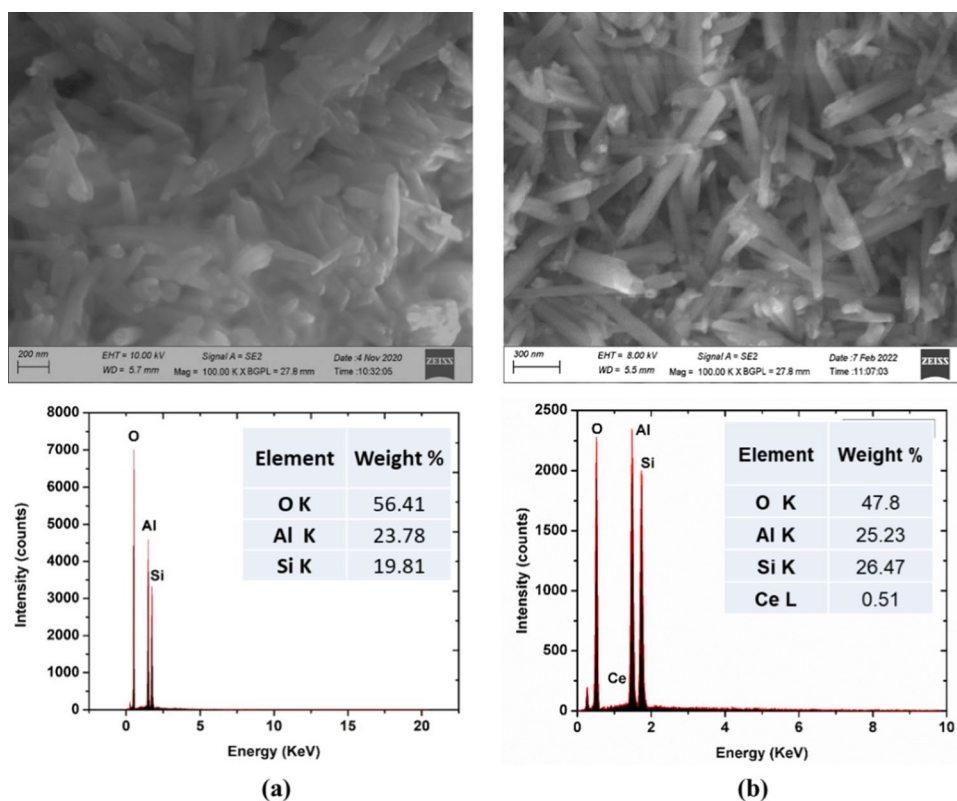## 3.1 Characterization of Inhibitor Loaded Nanocontainers

3.1.1 FESEM/EDS analysis

Surface morphology of the as-procured HNT and inhibitor loaded HNT was confirmed from SEM analysis. Elemental mapping of bare HNT and modified HNT confirms the presence of Al, Si, O and respective elements of each corrosion inhibitor, thereby confirming the encapsulation of corrosion inhibitors (CI) into HNTs. Figure 2a corresponds to bare HNT, where the morphology of HNT appears to be tubular and cylindrical. Figure 2b corresponds to cerium encapsulated HNT. The SEM and EDS analysis for other inhibitor encapsulated HNTs are presented in Fig. S1 (a) and (b) (supplementary data).
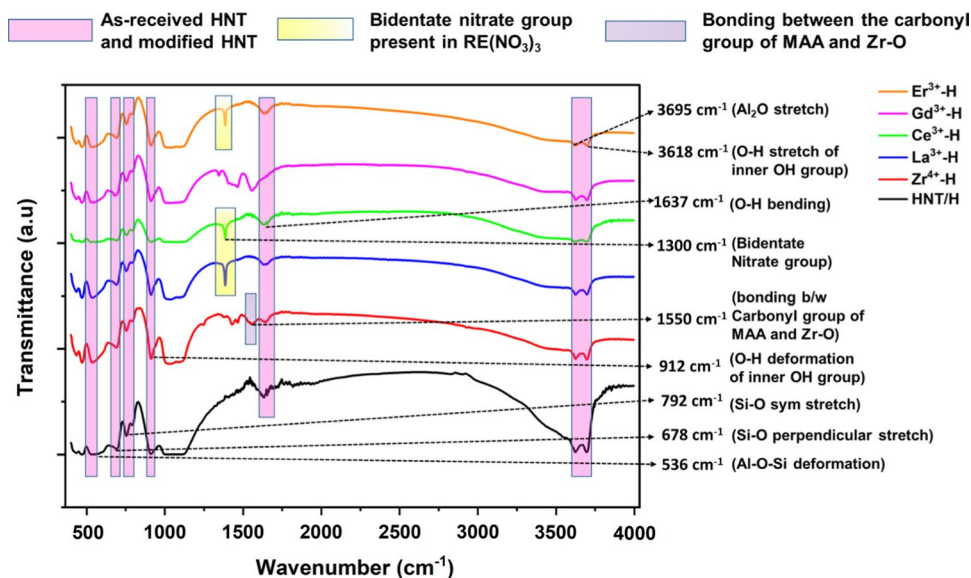
3.1.2 FTIR Analysis

FTIR spectra for bare HNT/H and inhibitor loaded HNT are shown in Fig. 3. The spectra for all the

Fig. 2 Surface morphology and EDS analysis of **a** as-received HNT powder and **b** Ce^{3+} loaded HNT powder

Element	Weight %
O K	56.41
Al K	23.78
Si K	19.81

Element	Weight %
O K	47.8
Al K	25.23
Si K	26.47
Ce L	0.51

(a)

(b)

Fig. 3 FTIR spectra of as-received HNT and modified inhibitor loaded HNT

inhibitor-modified HNT show a similar pattern as that of the bare HNT. The distinguished peaks at 3695, 3618, 1637, 912, 792, 678, and 536 cm^{-1} can be assigned to O–H stretching of inner surface hydroxyl groups, O–H stretching of inner hydroxyl groups, O–H deformation of water, O–H deformation of inner hydroxyl groups, symmetric Si–O stretching, perpendicular Si–O stretching and Al–O–Si deformation, respectively [25]. The peak at 1300 cm^{-1} is due to the bidentate nitrate present in RE(NO$_3$)$_3$ [26]. The evolved band at 1550 cm^{-1} is due to the bonding between the carbonyl group of MAA and Zr–O [27]. Comprehensively, FTIR analysis confirms the loading of corrosion inhibitors into the empty lumen of HNT.

3.1.3 XRD Analysis

Figure 4 depicts the XRD patterns of bare HNT and inhibitor-loaded HNT powders. The XRD patterns for inhibitor-modified HNT are in good agreement with that of the as-received HNT. The diffraction peaks for bare HNT are obtained at 12°, 21°, 24°, 25°, 28°, 34° and 37°, which are assigned to (002), (111), (004), (202), (113), (020) and (022) diffraction, respectively. According to ICDD file no. 01-77-4776, the structure of bare HNT was found to be monoclinic. The similar XRD pattern for all the inhibitor-loaded HNTs confirms that there is no change in the interlayer spacing between silica and alumina layers of HNT. The reason behind the peak broadening is due to the loading of corrosion inhibitor inside the HNT lumen. Full-width at half-maximum (FWHM) values for the prominent and symmetric basal peak at 12° are shown in Table 1. It may be noted that the FWHM values are higher for inhibitor loaded HNT when

compared to as-received HNT, confirming the loading inside the nanotube instead of intercalating in between the layers [28]. Supplementary data shows the crystallite size calculations consolidated in Table S1.

3.2 Characterization of HNT-Based Coatings

3.2.1 Thickness and Tape-Peel Off Test

The thicknesses of all the coatings measured using Posi-Tector® ranged from 4 to 8 μm. A tape peel-off test was performed to confirm the adhesion of the coatings. Representative results pertaining to CS and CHS coatings in the form of optical microscope images are shown in Fig. 5. The results for all other coatings are presented in Fig. S2. The images confirmed that all the coatings possess excellent adhesion and are categorized under 0 class, meaning 0% or no removal as per ISO standard 2409.

3.2.2 Water Contact Angle Measurements

The water contact angle measurement was carried out for both Z/RE and Z/REH-coated MS substrates. Researchers around the globe have reported different wettabilities of the RE-based coatings. Recently, a group of researchers have carried out significant experiments and confirmed that the coatings based on RE are initially hydrophilic, which later becomes hydrophobic. The increase in hydrophobicity was explained as due to the absorption of hydrocarbons from the surrounding environment [29]. Similar results were obtained in our measurements. The water contact angle was found to decrease for all the RE-based coatings when compared to matrix sol-coated substrates, as shown in Fig. 6 and S3. The WCA for ZHS coating was comparatively high for direct
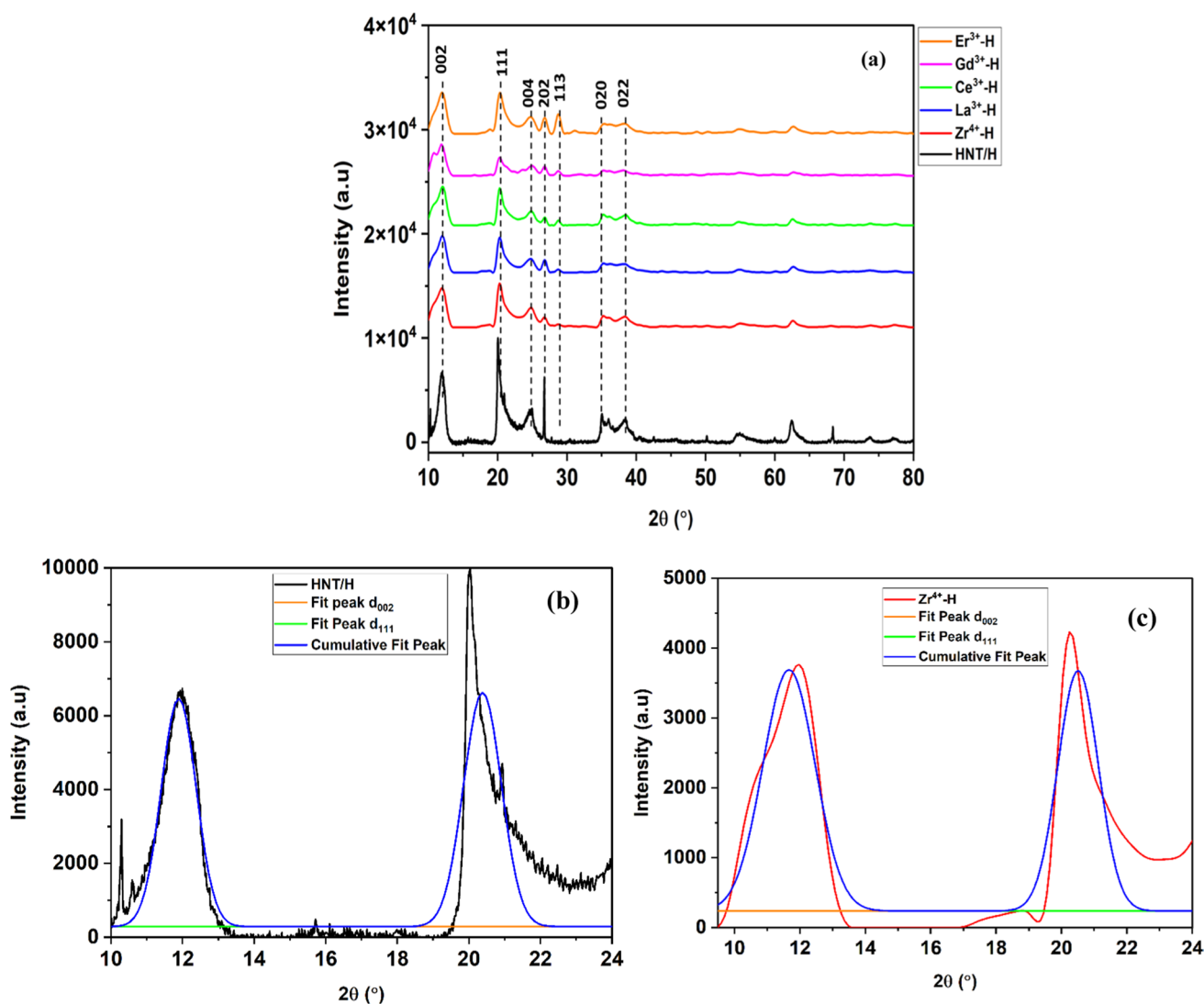
Fig. 4 **a** XRD patterns for as-received HNT and different inhibitor loaded HNTs; Normalized XRD peaks of d_{001} and d_{002} planes of **b** as-received and **c** inhibitor loaded and stoppered halloysite nanotubes for the calculation of FWHM values

Table 1 FWHM values of (002) peak of as-received and inhibitor loaded HNTs

| Sample Name	FWHM values
As-received HNT(H)	1.127°
Zr^{4+}-H	1.836°
La^{3+}-H	1.854°
Ce^{3+}-H	1.700°
Gd^{3+}-H	1.928°
Er^{3+}-H	1.677°

addition and encapsulation. The reason behind this increase is the presence of MAA in the coatings, which leads to the formation of long organic chains at the time of curing. Increased hydrophobicity in the case of ZHS can be due to

the surface modification of HNT caused during loading of zirconium-n-propoxide into HNT, which has adsorbed more on the surface rather than loading into the lumen. As the outer surface of HNT is negatively charged, the adsorption of Zr^{4+} ions outside is relatively more when compared to loading into the HNT. Detailed explanation for this behaviour is explained in the electrochemical section [23].

3.2.3 Electrochemical Impedance Spectroscopy (EIS) and Potentiodynamic Polarization Studies (PPS)

3.2.3.1 Effect of Direct Addition of Rare-Earth Corrosion Inhibitors Into the Matrix Sol Nyquist plots obtained for bare and different Z/RE-coated MS substrates after exposure to 0.6 M sodium chloride solution for 1 h are shown in Fig. 7. From the figure, it is evident that the impedance for
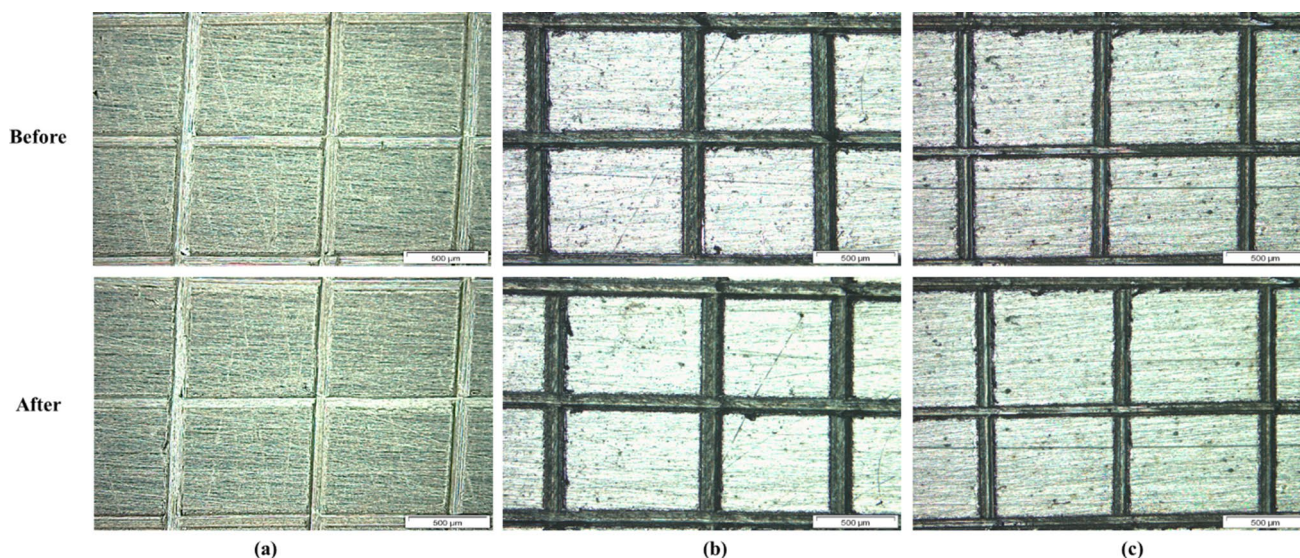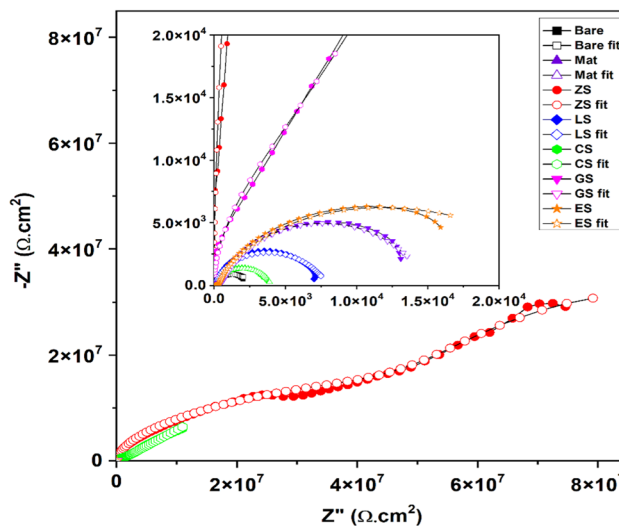
Fig. 5 Optical images of before and after tape adhesion test for MS substrates coated with **a** Matrix, **b** CS and **c** CHS. The bars given in the images represent 0.5 mm
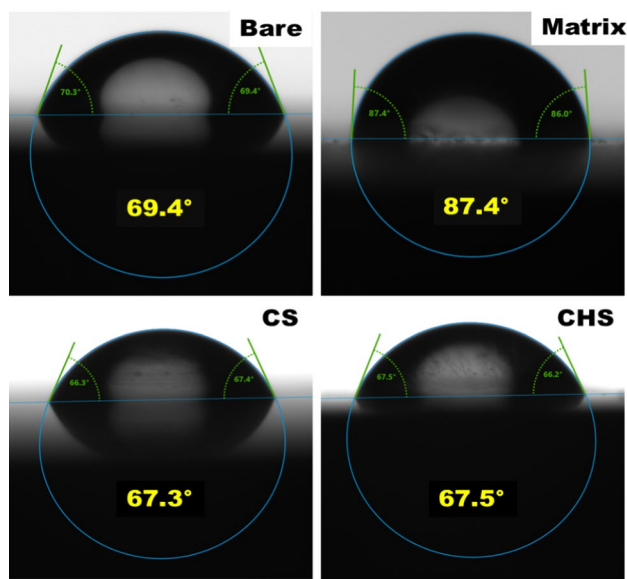
Fig. 6 Water drop images for bare and coated MS substrates

Fig. 7 Nyquist plots for bare and RE-coated MS substrates after immersion in 0.6 M sodium chloride solution for 1 h

ZS coated MS was very high followed by CS. The imped-ance data of CS coated MS substrate was fitted using three-time constants as shown in Fig. 1 b. The other RE-coated MS substrates have performed nearly the same; no major difference was observed in the corrosion resistance values.

The fitting parameters for bare and RE-coated substrates are shown in Table 2. The charge transfer resistance value for ZS coating was the highest i.e., 4.88×10^7 $\Omega.cm^2$ when compared to other coatings, suggesting that this coating pos-sesses high barrier properties.

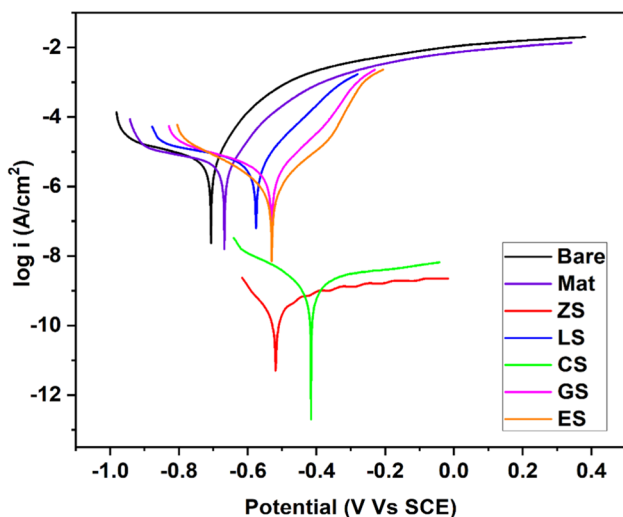Tafel plots for bare and Z/RE-coated substrates after immersion in 0.6 M sodium chloride solution are shown in Fig. 8. The polarization fit parameters are consolidated in Table 3. The corrosion potential values have shifted to more positive potentials for all coatings when compared to bare and matrix coated MS. Hence, all the coatings firmly exhibit the self-healing action as and when the corrosion process initiates. The current density value was least for ZS coatings followed by CS, which is the same trend as obtained in the EIS measurements.

The main reason for the increased coating performance of ZS is due to the presence of epoxide group in GPTMS,
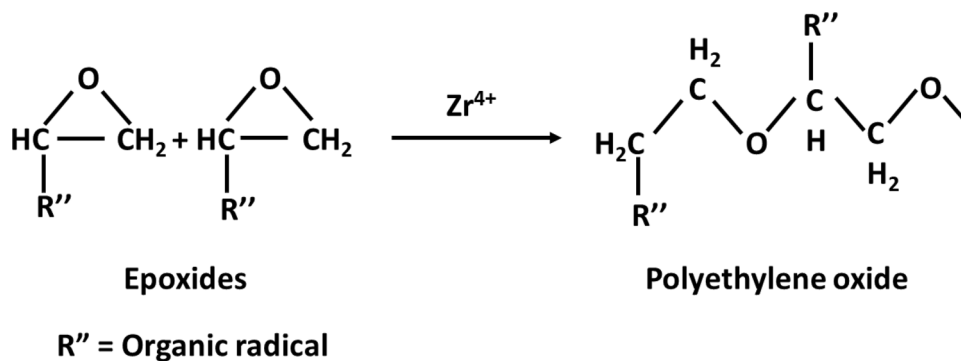
Table 2 Fit parameters obtained for electrochemical impedance data after 1 h immersion of bare and coated MS in 0.6 M sodium chloride solution

Sample	R_{coat} ($\Omega.cm^2$)	R_{ct} ($\Omega.cm^2$)	R_{diff} ($\Omega.cm^2$)	C_{coat} (F/cm^2)	C_{edl} (F/cm^2)	C_{diff} (F/cm^2)	CHI^2
Bare	–	2558	–	–	4.28×10^{-4}	–	5.36×10^{-3}
Matrix	158.1	3813	–	1.59×10^{-5}	5.61×10^{-5}	–	3.57×10^{-3}
ZS	2557	4.88×10^7	–	4.13×10^{-10}	2.05×10^{-8}	–	3.28×10^{-3}
CS	2.215×10^4	6.10×10^5	6.46×10^8	2.26×10^{-10}	9.00×10^{-10}	0.001296	4.05×10^{-3}
ES	425.5	2.63×10^4	–	92.35×10^{-6}	4.71×10^{-5}	–	4.01×10^{-3}
GS	785.2	1.42×10^4	–	4.59×10^{-6}	7.25×10^{-5}	–	6.88×10^{-3}
LS	124.7	7865	–	4.11×10^{-6}	2.76×10^{-5}	–	9.89×10^{-3}

Fig. 8 Tafel plots for bare and RE-coated MS substrates after immersion in 0.6 M sodium chloride solution for 1 h

Table 3 Tafel fit parameters obtained for potentiodynamic polarization data after 1 h immersion of bare and coated MS in 0.6 M sodium chloride solution

Sample	E_{corr} (V Vs SCE)	I_{corr} (A/cm^2)	R_p ($\Omega\ cm^2$)
Bare	-0.707	5.54×10^{-6}	4566
Matrix	-0.668	5.37×10^{-6}	6098
ZS	-0.519	0.00017×10^{-6}	93,281,608
LS	-0.576	4.57×10^{-6}	7244
CS	-0.416	0.0018×10^{-6}	26,659,758
GS	-0.530	2.51×10^{-6}	12,044
ES	-0.547	1.58×10^{-6}	19,220

The CS-coated substrates have shown an increase in charge transfer resistance and a decrease in current density because of the formation of a thick layer of cerium hydroxide and cerium oxide on the MS substrate. This thick layer contributes to the increased barrier properties, which in turn passivates the MS surface and inhibits the entry of chloride ions into the coating [31]. This is the reason why the EIS data for CS coated substrates was fitted using three-time constants. LS, GS and ES have shown an increase in corrosion resistance based on their oxide formation. The stability of oxide formation of RE_2O_3 increases on moving left to

which is the primary constituent material. in the matrix sol, and has high activity in presence of zirconium. The zirconium helps polymerise the epoxide ring into polyethylene oxide, which in turn forms a long polymer chain, hence providing excellent barrier and self-healing properties [30].

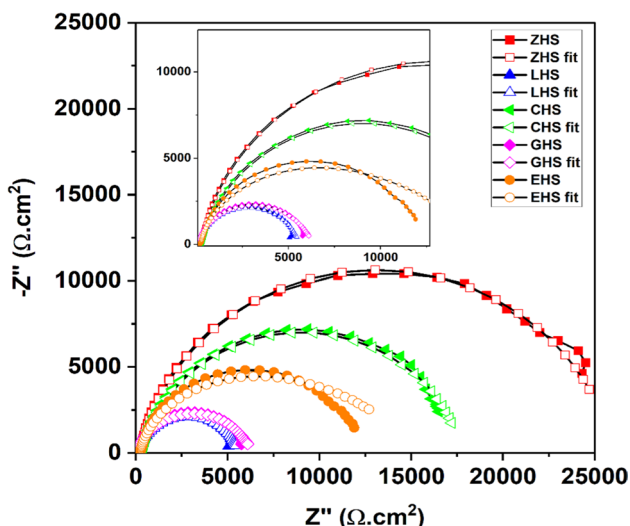Epoxides   Polyethylene oxide

R'' = Organic radical

Fig. 9 Nyquist plots for different inhibitor loaded HNT sol coated MS substrates after immersion in 0.6 M sodium chloride solution for 1 h

Fig. 10 Tafel plots for different corrosion inhibitor loaded HNT sol coated MS substrates after immersion in 0.6 M sodium chloride solution for 1 h

right in the periodic table due to lanthanide contraction and decrease in ionic size, and therefore, the order of charge transfer resistance follows ES > GS > LS [32].

3.2.3.2 Effect of Encapsulation of Rare-Earth-Based Corrosion Inhibitors Into HNT Followed by Dispersion into the Matrix Sol

To observe the effect of encapsulation of corrosion inhibitors into nanocontainers, all the corrosion inhibitors used in our study were loaded into HNTs. Encapsulated HNT-derived sol-coated MS substrates were then exposed to 0.6 M sodium chloride solution for 1 h. Nyquist plots obtained are shown in Fig. 9, and the impedance data fit parameters are tabulated in Table 4. It is clear from the Nyquist plots that the ZHS coating has shown an increase in impedance values suggesting improved coating performance against corrosion. The other REH-coated substrates have shown lower impedance values when compared to ZHS samples. EIS fit parameters also show that the charge transfer resistance of the ZHS coating was highest among all REH-coated MS substrates.

To complement the electrochemical data, polarization studies were carried out. Figure 10 shows the Tafel plots for the coatings mentioned above, where the current density values for all the coatings are of the same order, i.e., 10^{-6} A/
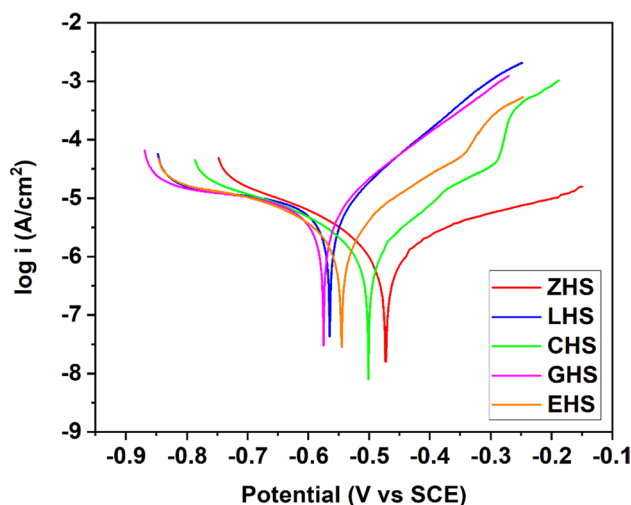
cm^2. The only difference was in the magnitude of the current density for all the coatings. The polarization fit data is consolidated in Table 5. The current density value for the ZHS coated sample was the least, revealing that the coating is intact and thereby restricting the entry of electrolyte species. The order of decreasing corrosion protection is as follows: ZHS > CHS > EHS > GHS > LHS.

3.2.3.3 Comparison of Direct Addition of Corrosion Inhibitors and Encapsulation of Corrosion Inhibitors Into HNT

Individual plots were drawn to easily compare and analyze the Nyquist and Tafel plots of each inhibitor when directly dispersed or encapsulated into HNT, as shown in Fig. S4 (i to v). To confirm the coating resistance and self-healing action of all the coating formulations applied on MS substrates, charge transfer resistance and current density data for direct addition and for encapsulation of corrosion inhibitor into the HNT are compared in Fig. 11a and b, respectively. It is clear from Fig. 11a that the charge transfer resistance values for direct addition of corrosion inhibitor-based sol-coated substrates have performed well when compared to encapsulation of corrosion inhibitor into HNTs. Similarly, the current density values for direct addition have

Table 4 Fit parameters obtained for electrochemical impedance data after 1 h immersion of bare and coated MS in 0.6 M sodium chloride solution

Sample	R_{coat} ($\Omega.cm^2$)	R_{ct} ($\Omega.cm^2$)	C_{coat} (F/cm^2)	C_{edl} (F/cm^2)	CHI^2
ZHS	166.4	2.58×10^4	5.84×10^{-9}	7.53×10^{-5}	2.55×10^{-3}
CHS	306.7	1.75×10^4	1.79×10^{-8}	6.56×10^{-5}	0.66×10^{-3}
EHS	274.8	1.64×10^4	5.89×10^{-8}	6.21×10^{-5}	1.34×10^{-3}
GHS	77.61	6247	2.95×10^{-6}	6.61×10^{-5}	6.05×10^{-3}
LHS	39.23	5506	1.27×10^{-6}	1.21×10^{-4}	7.37×10^{-3}

Table 5 Tafel fit parameters obtained for potentiodynamic polarization data after 1 h immersion of bare and coated MS in 0.6 M sodium chloride solution

Sample	E_{corr} (V Vs SCE)	I_{corr} (A/cm^2)	R_p ($\Omega.cm^2$)
ZHS	− 0.472	1.25×10^{-6}	30,240
CHS	− 0.501	1.53×10^{-6}	20,582
EHS	− 0.545	2.65×10^{-6}	13,159
GHS	− 0.575	6.33×10^{-6}	6048
LHS	− 0.565	6.83×10^{-6}	5495

shown lower values when compared to those obtained for encapsulation of corrosion inhibitor into the HNTs.

The HNTs are composed of aluminosilicate layers, where the external surface is negative in charge forming Si–O–Si network and the positively charged inner surface of Al–OH groups [33]. The inner arrangement of Al–OH groups is like an erected triangle where the top head comprises Al^{3+} ions protruding away from the tube's inner lining, and OH– ions are the two ends of the triangle attached to the surface of the inner tube, making the lumen positively charged from inside, as shown in Fig. 11c [23].

The inorganic/rare earth elements being cationic and hydrophilic makes it difficult to form a chemical bond with the Al^{3+} ions and may not completely load in the empty and positively charged lumen of HNT. Thus, loading efficiency may be less when compared to other organic molecules. On the other hand, the adsorption of these inorganic or RE on the outer surface of HNT is more prominent due to the affinity towards the hydroxyl group present on the outer surface. Therefore, during the corrosion process, these ions are
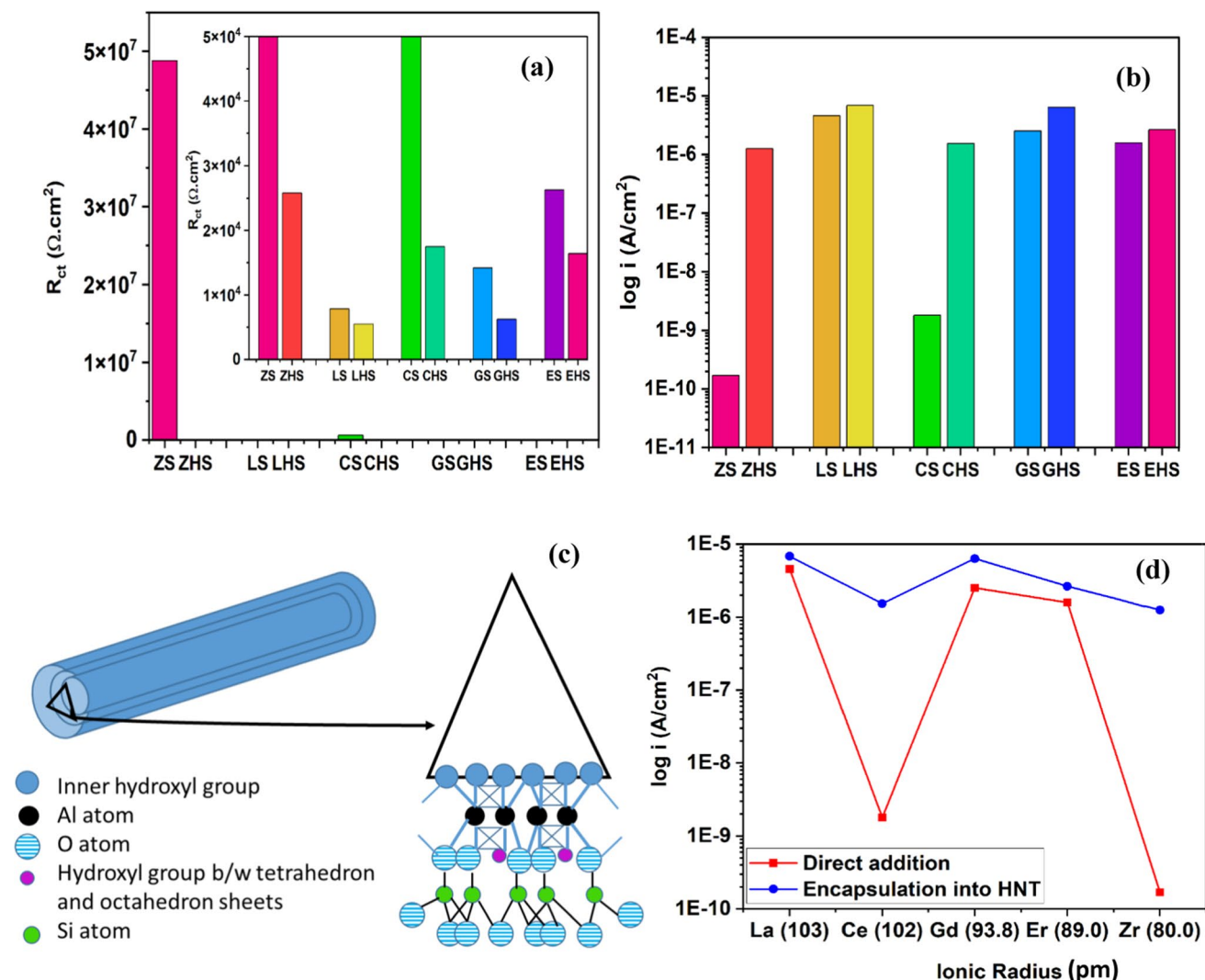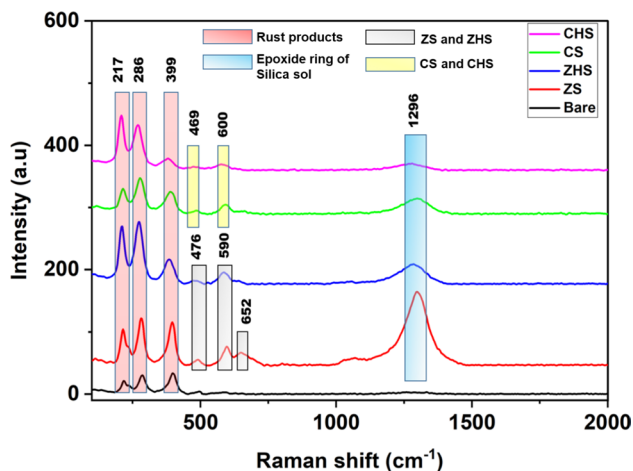

Fig. 11 **a** comparison of charge transfer resistance, **b** comparison of current density, **c** schematic representation of structure of halloysite nanotube, and **d** current density plot w.r.t ionic radius for direct and corrosion inhibitor loaded HNT sol-coated MS substrates after immersion in 0.6 M sodium chloride solution for 1 h

released slowly, thereby showing lesser corrosion protection when compared to direct addition [34]. On direct addition, these inorganic or cationic corrosion inhibitors are in close vicinity and show an immediate reaction to any stimuli caused due to corrosion thus ensuring quick healing action by forming a stable oxide film on the mild steel surface. The trend of corrosion protection for direct addition and encapsulation is still the same. Corrosion protection decreases with decrease in the ionic radius of the constituent ions i.e., $Zr^{4+} > Ce^{3+} > Er^{3+} > Gd^{3+} > La^{3+}$. Figure 11d shows the comparison of direct addition and encapsulation of corrosion inhibitors into HNT w.r.t ionic radius schematic of HNT.

3.2.4 Micro Raman Spectroscopic Analysis

In order to evaluate the self-healing action, Micro-Raman spectroscopic studies for bare, zirconium and cerium-coated MS samples were carried out on scribed bare and coated MS substrates, after exposure to 0.6 M sodium chloride solution for 1 h. The Micro-Raman spectra were obtained for the scribed region and are shown in Fig. 12. Table 6

Fig. 12 Micro-Raman spectra for bare and coated substrates obtained after exposing the substrates in 0.6 M sodium chloride solution for 1 h
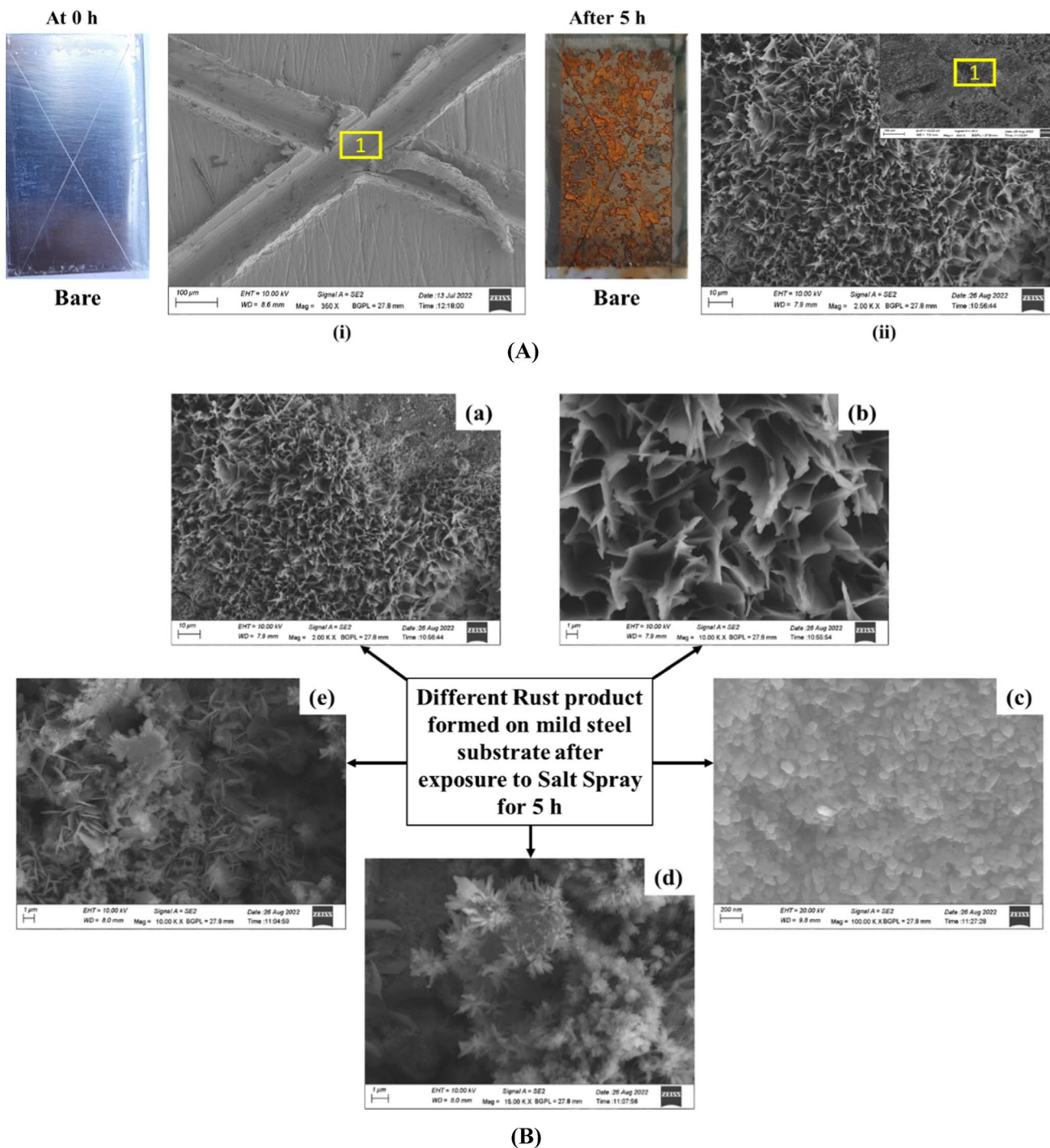
shows the peak shifts corresponding to different compounds in bare and coated MS substrates. It should be noted that the peaks observed for bare MS substrates are quite distinct in the scribed region of the other coated MS substrates as well. The Raman analysis also confirms the self-healing action of the corrosion inhibitors, as Zr^{4+} and Ce^{3+}/Ce^{4+} ions have been released in the scribed region and form a passive film by forming stable oxides of CeO_2 and ZrO_2. Salt spray analysis in the next section will provide a clear picture of the surface morphology of the rust products and self-healing products formed on bare and coated substrates after salt spray exposure.

3.2.5 Salt Spray Test

Bare and coated MS substrates were exposed to salt spray for 5 h as per ASTM B117 standard. The bare and coated substrates were cross-scribed and photographs were collected before and after exposure to the salt spray test (SST). FESEM/EDS analysis at 0 h (i.e. prior to SST) was employed to confirm the complete removal of coating by scribe process and that after 5 h SST to examine the self-healing action/ rust product formation. Photographic and SEM images of MS coupons coated with (i) matrix sol alone, (ii) transition or rare-earth metal directly added matrix sols, and (iii) transition or rare-earth metal encapsulated HNT added matrix sols were recorded before exposure to salt spray test and after 5 h exposure to salt spray test, and all they were shown in Figs. 13 and 14 and in Fig. S5(A) and (B). Point 1 in all the SEM images corresponds to the scan area where EDS analysis was carried out. Table 7 shows the EDS analysis in the scribed area for bare/coated substrates before and after exposure to SST. Tables S2 and S3 depict the EDS analysis data for other coatings. Figure 13A shows the images of bare substrates at 0 and 5 h. The SEM image at 0 h confirms the complete removal of the coating. After 5 h of exposure, the visual image shows that the surface has been completely corroded with maximum rust products on the surface. The Fig. 13B is an extended image of Fig. 13A (ii). In Fig. 13B, FESEM images of different rust products are observed on

Table 6 Raman peak shift for scribed coated and bare MS substrates after exposure to 0.6 M sodium chloride solution for 1 h

Compound	Coating	Peak shift (cm^{-1})	Reference
Lepidocrocite (γ-FeOOH)	Bare and coated MS	217	[35, 36]
Hematite (α-Fe$_2$O$_3$)	Bare and coated MS	286	[35, 36]
Goethite (α-FeOOH)	Bare and coated MS	399	[35, 36]
Epoxide ring of silica sol involved in polymerization	coated MS substrates	1296	[37]
Tetragonal ZrO$_2$	ZS and ZHS	652 and 590	[38, 39]
Monoclinic ZrO$_2$	ZS	476	[40]
Fluorite structure of CeO$_2$	CS and CHS	469	[41, 42]
Reduction of Ce^{4+} to Ce^{3+}	CS and CHS	600	[41, 42]

Fig. 13 A Visual and FESEM image of bare substrate before and after exposure to salt spray; **B** corrosion products formed on bare MS: **a** and **b** Lepidocrocite; **c** Goethite and **d** and **e** Akaganeite, respectively

bare MS substrates. The FESEM data is in good agreement with the Micro-Raman spectroscopy data. In Fig. 13B, images (a) and (b) correspond to needle-like sharp structures of Lepidocrocite. Figure (c) shows more of round cotton ball structures which resemble and represent Goethite, and Figure (d) and (e) have nearly same morphological structures

which resembles rosette morphology of Akaganeite. Lepidocrocite, goethite and akaganeite are different crystalline structures of iron-oxyhydroxide (FeO(OH)). Lepidocrocite (γ-FeO(OH)) forms when iron-containing substances rust in underwater conditions, and goethite is the main component of rust. Akaganéite (β-FeOOH, Cl) is a relatively rare iron
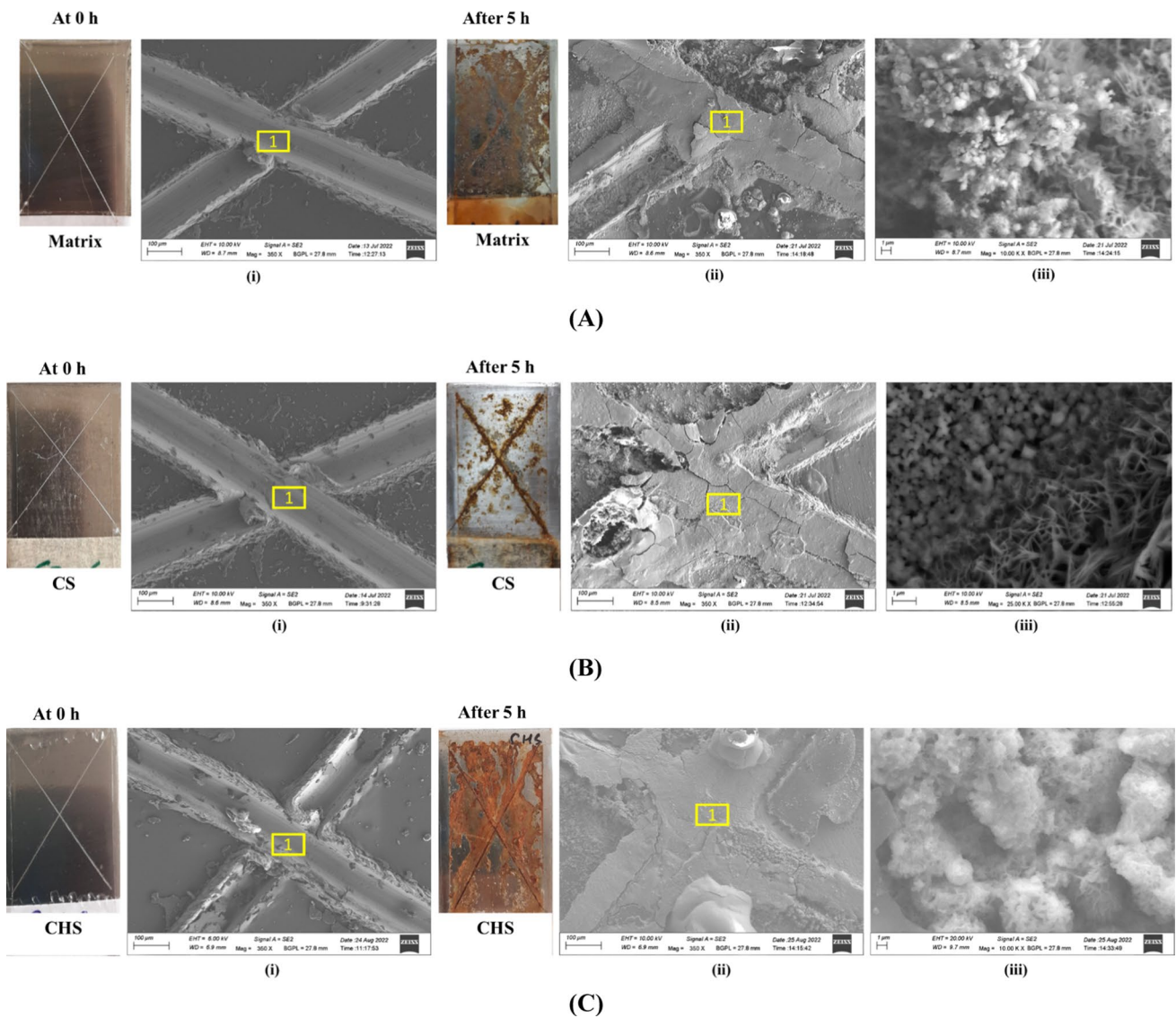
Fig. 14 Visual and FESEM images of **A** Matrix-coated, **B** CS-coated MS and **C** CHS-coated MS before and after exposure to salt spray

Table 7 EDS analysis for bare and coated MS substrates before and after exposure to SST

Sample Name	SST	C	O	Al	Si	Fe	Ce
Bare	Before	2.88	1.55	–	–	95.57	–
	After	–	25.92	–	–	74.08	–
Matrix	Before	2.51	2.63	–	0.27	94.59	–
	After	5.65	44.47	–	0.48	49.40	–
CS	Before	2.73	1.28	–	0.32	95.67	–
	After	4.02	33.64	–	1.37	60.02	0.95
CHS	Before	0.21	0.66	–	0.29	98.84	–
	After	1.21	21.65	0.09	0.97	75.53	0.55

oxyhydroxide that is found in chloride-rich environments such as marine environments. The observed different crystalline forms of rust are very much relevant to the experimental conditions of salt spray test, where the specimens were under high concentrations of chloride. High magnification FESEM images (Fig. 13B) are in good agreement with the results of

Micro-Raman spectroscopy analysis. These rust products are different stages of iron oxide which undergo phase transformation as the corrosion process initiates [43–46].

Figure 14A shows the image of matrix-coated MS substrates, where the surface after 5 h exposure looks similar as that of bare MS. The FESEM image at higher magnification shows the silica nanoparticles and Lepidocrocite structures in the scribed area (iii). For CS coatings, as shown in Fig. 14B, image (i) presents the FESEM image at 0 h, and images (ii and iii) present FESEM images after 5 h. The corrosion products were prominent in the scribed area and on the surface adjacent to the scribed area, whereas with lesser rust products on all the other surface areas. Figure (ii) shows that the scribed area has been healed by forming a thick layer. Figure (iii) shows the FESEM image of the scribed area at a higher magnification, where cuboidal crystal structures correspond to CeO_2 and the rust product in the right-most corner belongs to the Lepidocrocite structure. Figure 14C shows the visual and FESEM images of CHS-coated MS substrates. The surface shows the rust products in the form of patches. FESEM image (ii) confirms that the self-healing layer have formed partially on the cross scribed zone when compared to CS coated MS. It is clear from Fig. (iii) that the self-healing material and the rust product co-exist together, where the spherical structures of insoluble CeO_2 [47] are covered with a thin film of Akaganeite structure.
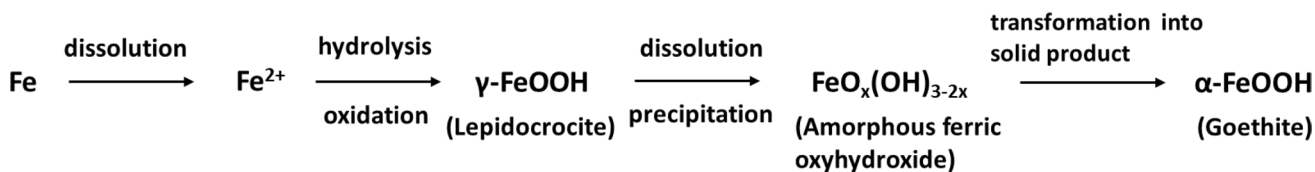
Figure S5 (A) shows the consolidated data for Z/RE-coated and (B) Z/REH-coated MS substrates. Photographic images showed that MS substrates coated with transition or rare-earth metal added matrix sols have exhibited more stability against corrosion compared to MS substrates coated with transition or rare-earth metal encapsulated HNT added matrix sols. The SST confirmed that the self-healing action of direct addition of corrosion inhibitor is more when compared to the encapsulation of corrosion inhibitor into HNT. Visual and FESEM images for both the coating types clearly show that the rust product in the scribed area and on the surface of the coated samples are more on the halloysite-based coatings rather than the direct inhibitor-loaded coatings. The elemental analysis also supports this, as the rust product elements i.e., Fe and O have shown increase in weight % in the scribed area for Halloysite-based coatings compared to direct addition. The trend for corrosion protection for direct addition is as follows: LS > GS > ES > CS > ZS > Matrix > Bare and for encapsulation into HNT is: LHS > GHS > EHS ≈ ZHS > CHS. The results of SST analysis were firmly supported by the results of electrochemical impedance and potentiodynamic polarization studies carried out after 1 h immersion in 0.6 M NaCl solution (Figs. 7, 8, 9 and 10,

Tables 2, 3, 4, 5), which demonstrated superior corrosion resistance for MS substrates coated with transition or rare-earth metal added matrix sols without any encapsulation process.

3.2.6 Comparison of Data From Electrochemical and Salt Spray Tests

From the electrochemical studies and salt spray test, it can be concluded that the direct addition of corrosion inhibitor into matrix sol coated MS substrates have provided better barrier as well as self-healing properties when compared to encapsulation of these corrosion inhibitors into HNTs. On close analysis, it can be observed that the trend of corrosion inhibition between the two techniques, i.e. the direct addition or the encapsulation, is far different. Electrochemical studies confirm that the zirconium-based coatings gave better corrosion performance, whereas, in SST, lanthanum-based coatings have shown decreased corrosion rate. The data obtained in the electrochemical technique is basically about the interface chemistry between the coating and the substrate which provides quantitative test results. The charge transfer resistance values give insight into the coating performance and adherence to the metal substrate. The corrosion inhibitor is released only when there is a coating breakdown. Usually, during polarization studies, the coating breaks down on the application of external voltage, and then the inhibitor is released, followed by the self-healing mechanism. SST describes the change on the surface of the substrate when exposed to an aggressive salt environment. During exposure in the SS chamber, the electrolyte (5 wt% NaCl solution) layer is continuously refreshed on the substrate, and the effect of the inhibitor may differ at each time [48, 49]. In SST, the continuous fogging leads to the formation of rust product initially in the scribed area, followed by self-healing action of the corrosion inhibitor or vice-versa. As evident from SST FESEM images, it was observed that the rust product is beneath the thick self-healing layer in the cross-scribed.

During initial exposure, the rust product must have covered the exposed area and slowly, the inhibitor from the near scribed area came into the picture initiating the passive film growth. This process goes on till the corrosion inhibitor is completely consumed. Another reason to explain the effect of coated samples in SS is the Lepidocrocite structure formation. During corrosion process, the γ-FeOOH is formed after the dissolution of Fe^{2+} ions followed by the formation of amorphous FeOOH. The final product is Goethite, α-FeOOH; a solid-state transformation. The other rust products are formed in between these two significant phases.

$$Fe \xrightarrow{\text{dissolution}} Fe^{2+} \xrightarrow[\text{oxidation}]{\text{hydrolysis}} \gamma\text{-FeOOH} \xrightarrow[\text{precipitation}]{\text{dissolution}} FeO_x(OH)_{3-2x} \xrightarrow{\substack{\text{transformation into} \\ \text{solid product}}} \alpha\text{-FeOOH}$$

$$\text{(Lepidocrocite)} \qquad \text{(Amorphous ferric oxyhydroxide)} \qquad \text{(Goethite)}$$

Therefore, in all the coated substrates after exposure to SST, the most significant rust product was γ-FeOOH confirming that the corrosion process is still at its onset, which is suppressed by the self-healing agents added into the coating matrix. The difference is just that the SST gives real-time test results, whereas, electrochemical studies provide results based on the sensitivity of the interface during the corrosion process.

Since SST is an accelerated test, the corrosion is faster during the salt spray test than during the polarization and electrochemical impedance studies. As a result, we see iron oxidation products first, followed by self-healing products formed by corrosion inhibitor migration. Furthermore, the direct addition of a corrosion inhibitor is more effective since migration of CI from the matrix is faster than from the narrow lumen of HNT. Figure 15 shows the schematics
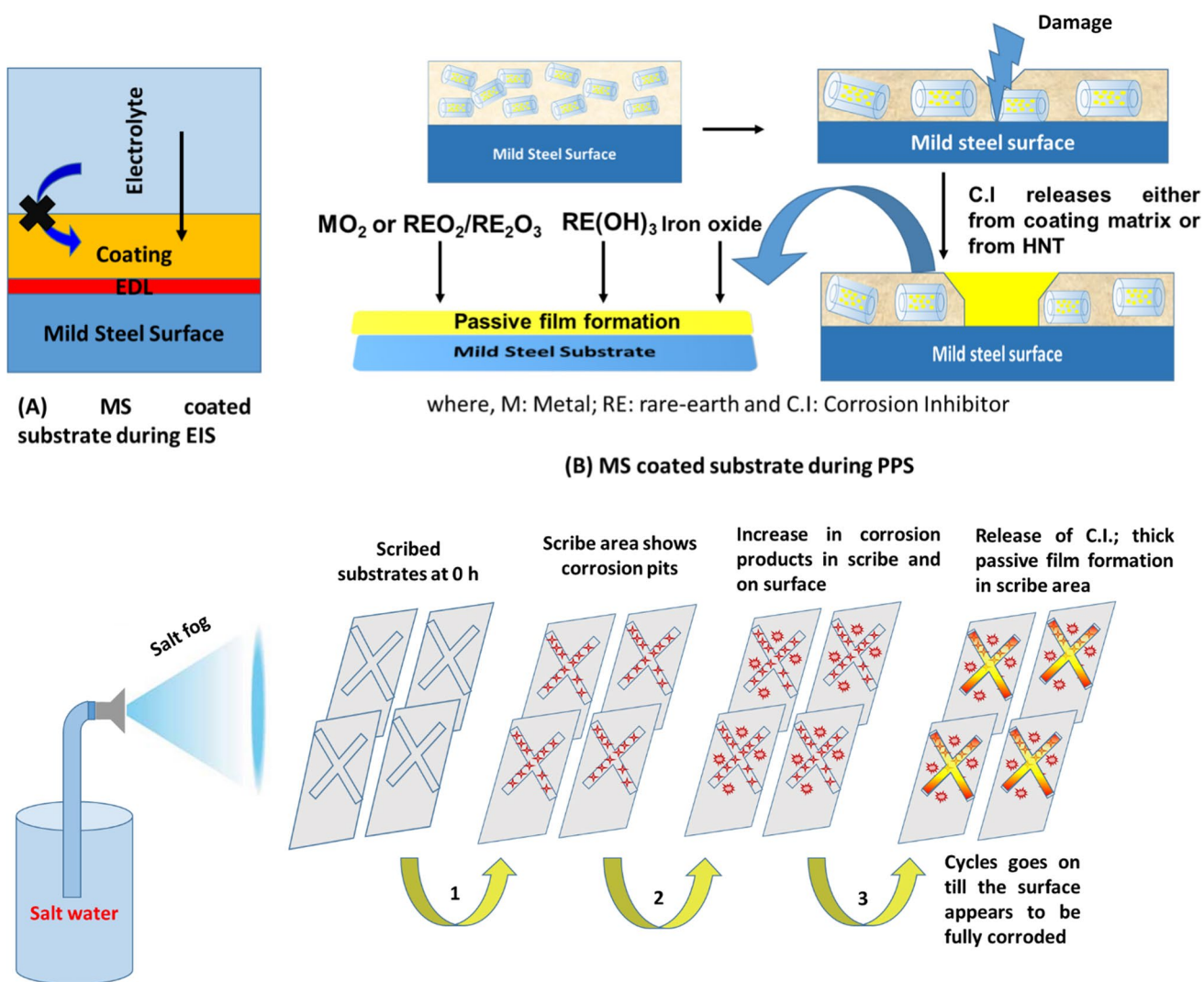

Fig. 15 Schematics of MS coated substrates during exposure to different corrosion techniques

of coated mild steel substrate when exposed to different corrosion methods.

4 Conclusions

- The present investigation confirmed that the silica sol consisting of inorganic corrosion inhibitors, i.e., transition metal and rare-earth elements, showed self-healing action on mild steel substrates.
- Electrochemical studies reveal that ZS coatings have shown better corrosion resistance when compared to other RE based coatings and the current density has decreased from 10^{-6} A/cm^2 for all other coatings to 10^{-10} A/cm^2 for ZS coatings.
- Coatings based on encapsulation of CI into HNT confirmed that the ZHS coating performed well in terms of corrosion resistance and self-healing action among all other REH-based coatings.
- Micro-Raman spectroscopic analysis for cerium and zirconium based coatings reveal that the inhibitor metal oxides are found in the scribed area, confirming the passive film formation leading to self-healing of the damaged region.
- Salt spray test revealed that the coatings based on direct addition of corrosion inhibitors into the sol exhibited higher corrosion resistance compared to encapsulation. The FESEM images confirmed that the corrosion is more pronounced on HNT-based coatings.
- All the investigations confirmed that the direct addition of inorganic corrosion inhibitors into the coating matrix exhibits higher corrosion protection compared to encapsulation based coatings.

Declarations

Conflict of interest On behalf of all authors, the corresponding author states that there is no conflict of interest.

References

1. D.T. Oyekunle, O. Agboola, A.O. Ayeni, J. Phys. Conf. Ser. **1378**, 32046 (2019)
2. O.S.I. Fayomi, A.P.I. Poppola, J. Phys. Conf. Ser. **1378**, 22006 (2019)
3. A.E. Somers, B.R.W. Hinton, C.B. Dickason, G.B. Deacon, P.C. Junk, M. Forsyth, Corros. Sci. **139**, 430 (2018)
4. J. Sinko, Prog. Org. Coat. **42**, 267 (2001)
5. P. Rodic, A. Mertelj, M. Borovsak, A. Bencan, D. Mihailovic, B. Malic, I. Milosev, Surf. Coat. Technol. **286**, 396 (2016)
6. A.M. Santos, I.P. Aquino, F. Cotting, I.V. Aoki, H.G. de Melo, V.R. Capelossi, Met. Mater. Int. **27**, 1519 (2021)
7. B. Chugh, A.K. Singh, S. Thakur, B. Pani, A.K. Pandey, H. Lgaz, I.M. Chung, E.E. Ebenso, J. Phys. Chem. C. **123**, 22897 (2019)
8. G.T. Galo, A.A. de Morandim-Giannetti, F. Cotting, I.V. Aoki, I.P. Aquino, Met. Mater. Int. **27**, 3238 (2021)
9. A.S. Fouda, H. Megahed, D.M. Ead, Desalin. Water Treat. **51**, 3164 (2013)
10. M. Sanchez, M.C. Alonso, P. Cecilio, M.F. Montemor, C. Andrade, Cem. Concr. Compos. **28**, 256 (2006)
11. S. Roselli, M. Revuelta, C. Deya, R. Romagnol, Prog. Org. Coat. **174**, 107 (2023)
12. M.F. Momtemor, A.M. Simoes, M.G.S. Ferreira, Prog. Org. Coat. **44**, 111 (2002)
13. E. Shchukina, H. Wang, D.G. Shchukin, Chem. Commun. **55**, 3859 (2019)
14. A. Gavrilovic-Wohlmuther, A. Laskos, E. Kny, in *Corrosion Protection at the Nanoscale*, ed. by S. Rajendran, T.A. Nguyen, S. Kakooei, M. Yeganeh, Y. Li (Elsevier, Amsterdam, 2020), pp. 203–223
15. R.B. Figueira, I.R. Fontinha, C.J.R. Silva, E.V. Pereira, Coatings **6**, 12 (2016)
16. G. Yang, H. Ma, L. Yu, P. Zhang, J. Colloid. Interface Sci. **333**, 776 (2009)
17. M. Nawaz, N. Yusuf, S. Habib, R.A. Shakoor, F. Ubaid, Z. Ahmad, R. Kahraman, S. Mansour, W. Gao, Polymers **11**, 852 (2019)
18. G. Williams, S. Geary, H.N. McMurray, Corros Sci. **57**, 139 (2012)
19. B.D. Mert, B. Yazici, S.B. Lyon, Corros. Eng. Sci. Technol. **48**, 506 (2013)
20. A. Ghazi, E. Ghasemi, M. Mahdavian, B. Ramezanzadeh, M. Rostami, Corros. Sci. **94**, 207 (2015)
21. D. Fix, D.V. Andreeva, Y.M. Lvov, D.G. Shchukin, H. Möhwald, Adv. Funct. Mater. **19**, 1720 (2009)
22. A. Gautam, K.R.C. Soma Raju, K.V. Gobi, R. Subasri, in *Recent Trends in Electrochemical Science and Technology*, vol. 15, ed. by U. Kamachi Mudali, S.T. Aruna, H.P. Nagaswarupa, D. Rangappa (Springer, Singapore, 2022), pp. 1–15
23. Y. Lvov, W. Wang, L. Zhang, R. Fakhrullin, Adv. Mater. **28**, 1227 (2016)
24. A. Gautam, T. Siva, S. Sathiyanarayanan, K.V. Gobi, R. Subasri, Ceram. Int. **48**, 30151 (2022)
25. , M.E. R. Green, J.M. Hook, S.J. Antill, C.J. Kepert, J. Phys. Chem. C **112**, 15742 (2008)
26. S.K. Gupta, R. Gupta, B.G. Vats, J.S. Gamare, R.M. Kadam, J. Lumin. **235**, 118026 (2021)
27. P. Rodic, S. Zanna, I. Milosev, P. Marcus, Front. Mater. **8**, 756447 (2021)
28. A. Joshi, E. Abdullayev, A. Vasiliev, O. Volkova, Y. Lvov, Langmuir **29**, 7439 (2013)
29. J. Oh, D. Orejon, W. Park, H. Cha, S. Sett, Y. Yokoyama, V. Thoreton, Y. Takata, N. Miljkovic, iScience **25**, 103691 (2022)
30. I. Milosev, B. Kapun, P. Rodic, J. Iskra, J. Sol-Gel Sci. Technol. **74**, 447 (2015)
31. A. Dastgheib, M. Attar, A. Zarebidaki, Met. Mater. Int. **26**, 1634 (2020)
32. Y. Zhu, J. Zhuang, Y. Yu, X. Zeng, J. Rare Earths. **31**, 1 (2013)
33. E. Abdullayev, Y. Lvov, J. Mater. Chem. B. **1**, 2894 (2013)
34. M. Massaro, R. Noto, S. Riela, Catalysts **12**, 149 (2022)
35. D. de la Fuente, J. Alcantara, B. Chico, I. Diaz, J.A. Jimenez, M. Morcillo, Corros. Sci. **110**, 253 (2016)
36. V.L. Hostis, E. Amblard, W. Guillot, C. Paris, L. Bellot-Gurlet, Mater. Corros. **64**, 185 (2013)

37. M. Gnyba, M.J. Szczerska, M. Keranen, J. Suhonen, in *Proceedings of XVII IMEKO World Congress Metrology in the 3rd Millennium,* ed. by D. Ilić, M. Boršić, J. Butorac, IMEKO&HMD, Dubrovnik, 22-27 June 2003, p. 237

38. M.E. Manriquez, M. Picquart, X. Bokhimi, T. López, P. Quintana, J.M. Coronado, J. Nanosci. Nanotechnol. **8**, 6623 (2008)

39. D.V. Mashtalyar, I.M. Imshinetskiy, K.V. Nadaraia, A.S. Gnedenkov, S.L. Sinebryukhov, A.Yu. Ustinov, A.V. Samokhin, S.V. Gnedenkov, J. Magnes. Alloy. **10**, 513 (2022)

40. P. Ji, Z. Wang, X. Shang, Y. Zhang, Y. Liu, Z. Mao, X. Shi, Front. Chem. **7**, 245 (2019)

41. K. Aggoun, L. Chaal, J. Creus, R. Sabot, B. Saidani, M. Jeannin, Surf. Coat. Tech. **372**, 410 (2019)

42. N. Kainbayev, M. Sriubas, D. Virbukas, Z. Rutkuniene, K. Bockute, S. Bolegenova, G. Laukaitis, Coatings **10**, 432 (2020)

43. S. Fonna, Israr Bin M. Ibrahim, Gunawarman, S. Huzni, M. Ikhsan, S. Thalib, Heliyon **7**, e06608 (2021)

44. D. de la Fuente, I. Díaz, J. Simancas, B. Chico, M. Morcillo, Corros. Sci. **53**, 604 (2011)

45. J. Alcantara, D. de la Fuente, B. Chico, J. Simancas, I. Diaz, M. Morcillo, Materials **10**, 406 (2017)

46. K. Xiao, Z. Li, J. Song, Z. Bai, W. Xue, J. Wu, C. Dong, Met. Mater. Int. **27**, 2623 (2021)

47. P.P. Tumkur, N.K. Gunasekaran, B.R. Lamani, N.N. Bayon, K. Prabhakaran, J.C. Hall, G.T. Ramesh, Nanomanufacturing **1**, 176 (2021)

48. R.G. Buchheit, M. Cunningham, H. Jensen, M.W. Kendig, M.A. Martinez, Corrosion **54**, 61 (1998)

49. Z. Kefallinou, X. Zhou, M. Curioni, Surf Interface Anal. **51**, 1173 (2019)